

# The Influence of Molybdenum on Stainless Steel Weld Microstructures

*A method of producing austenitic welds is proposed that can potentially circumvent the difficulties normally encountered when fusion welding superaustenitic stainless steels*

BY T. D. ANDERSON, M. J. PERRICONE, J. N. DuPONT, and A. R. MARDER

**ABSTRACT.** Superaustenitic stainless steel alloys can often pose difficulties during fusion welding due to the unavoidable microsegregation of Mo and tramp elements, which lead to the loss of corrosion resistance and solidification cracking, respectively. A method of producing austenitic welds is proposed that can potentially circumvent these issues by designing fusion zone compositions that exhibit a primary ferrite solidification mode and subsequent solid-state transformation of ferrite to austenite. The ferritic solidification mode will minimize microsegregation during solidification due to elevated diffusion rates, while a subsequent solid-state transformation of ferrite into austenite will create the austenitic matrix that is desired for good toughness. Thermodynamic calculations were used to isolate the range of compositions over which this phase transformation sequence can occur in Fe-Ni-Cr-Mo alloys. Experimental stainless steel alloys with a wide range in Ni, Cr, and Mo concentrations were then prepared with an arc button melting technique to observe the microstructures and validate the thermodynamic diagrams. Four solidification modes (A, AF, FA, F) and three solid-state transformations ( $\delta \rightarrow \gamma$ ,  $\delta \rightarrow (\sigma+\gamma)$ , and  $\gamma \rightarrow$  martensite) were observed in this alloy system that produced a wide variety of microstructures. Good agreement was shown between experiment and thermodynamic calculations in the prediction of solidification mode. The amount of ferrite was also determined in each alloy via magnetic measurements. Empirical relations were assessed that relate the ferrite content to alloy composition, and the data were used for comparison with several weld constitution diagrams. Several alloys were identified that exhibited the desired transformation sequence. Electron probe

microanalysis measurements on these alloys confirmed that Mo was more uniformly distributed compared to alloys that solidified as austenite. Laser beam welds were also deposited on the surfaces of the button melts in order to observe the influence of higher cooling rates. While no solidification mode shifts occurred (with the possible exception of one alloy), the high cooling rate inherent to laser welding caused a  $\delta \rightarrow \gamma$  massive transformation. This massive structure exhibited an entirely austenitic microstructure with a uniform distribution of Mo at the nominal concentration.

## Introduction

An advanced class of materials known as superaustenitic stainless steel (SASS) has recently fallen into wider use due to its excellent corrosion resistance and toughness. The decreased maintenance costs associated with these materials have made them attractive to the pharmaceutical, food processing, and desalinization industries. One difficulty associated with the incorporation of SASS alloys has been the fabrication step of fusion welding. The melting and resolidification of these alloys has a considerable effect on mechanical and physical properties. Fusion welding is typically conducted on SASS alloys using high-Mo nickel-based filler metal alloys such as IN622 and IN625 (Ref. 1). The microsegregation of Mo solute produces Mo-depleted dendrite cores that show a greater susceptibility to localized corrosion (Ref. 2); the Ni-based filler metals contain high levels of Mo in order to help

compensate for this detrimental effect. Welding parameters have been shown to exhibit a significant effect on weld metal composition, segregation behavior, corrosion resistance, and weldability. Therefore, the processing parameters used during welding must be carefully controlled in order to ensure the deposition of welds that do not corrode easily or experience solidification cracking. Several of the effects that welding parameters and filler metal composition have on SASS fusion welds have been studied extensively and recently published (Refs. 1, 3, 4). From this research, it was shown that a number of practical problems accompany the use of the high-Mo, nickel-based filler metals that solidify in the fully austenitic mode, including dendritic core corrosion brought on by the unavoidable microsegregation of Mo during primary austenite solidification; relatively high solidification cracking susceptibility; high levels of precision are required of the welding parameters in order to attain the required weld composition; and a unit cost for the filler metal far beyond that of the stainless steel base metal, owing to the disproportionate levels of Ni and Mo present.

Dendrite tip undercooling associated with high-energy-density welding processes can potentially minimize or eliminate Mo microsegregation and the associated accelerated corrosion of the Mo-depleted dendrite cores. Recent research has shown that the corrosion resistance will be enhanced through the use of laser welding (Ref. 5). The microstructure that produces this effect can be attained through proper control of the laser processing parameters. Despite this improved corrosion resistance, the laser welding process is not without its practical limitations, which include the following: laser welds are not accommodating of all joint designs, particularly fillet welds; achieving the desired microstructure requires precise control of laser processing parameters and will depend on the plate thickness and joint design; implementing laser weld

## KEYWORDS

GTAW  
Molybdenum  
Superaustenitic Stainless Steel  
Solidification Cracking  
Cracking

T. D. ANDERSON, J. N. DuPONT, and A. R. MARDER are with Lehigh University, Bethlehem, Pa. M. J. PERRICONE is with RJ Lee Group, Inc., Pittsburgh, Pa.

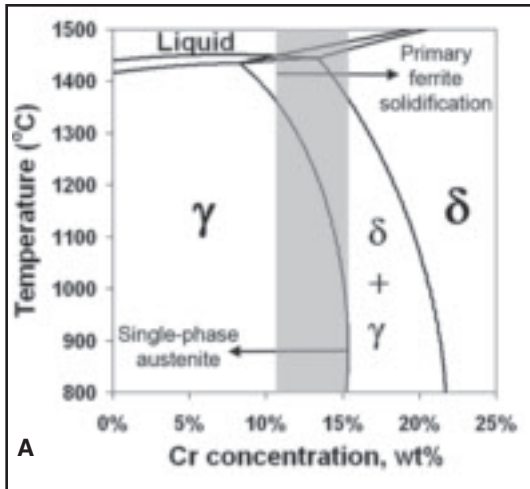


Fig. 1 — Separate views of the Fe-Ni-Cr-6Mo phase diagram. A — Vertical isopleth at 69 wt-% Fe; B — phase stability diagram highlighting Fe-Ni-Cr compositions with 6 wt-% Mo. The compositional zone of interest is highlighted in both diagrams.

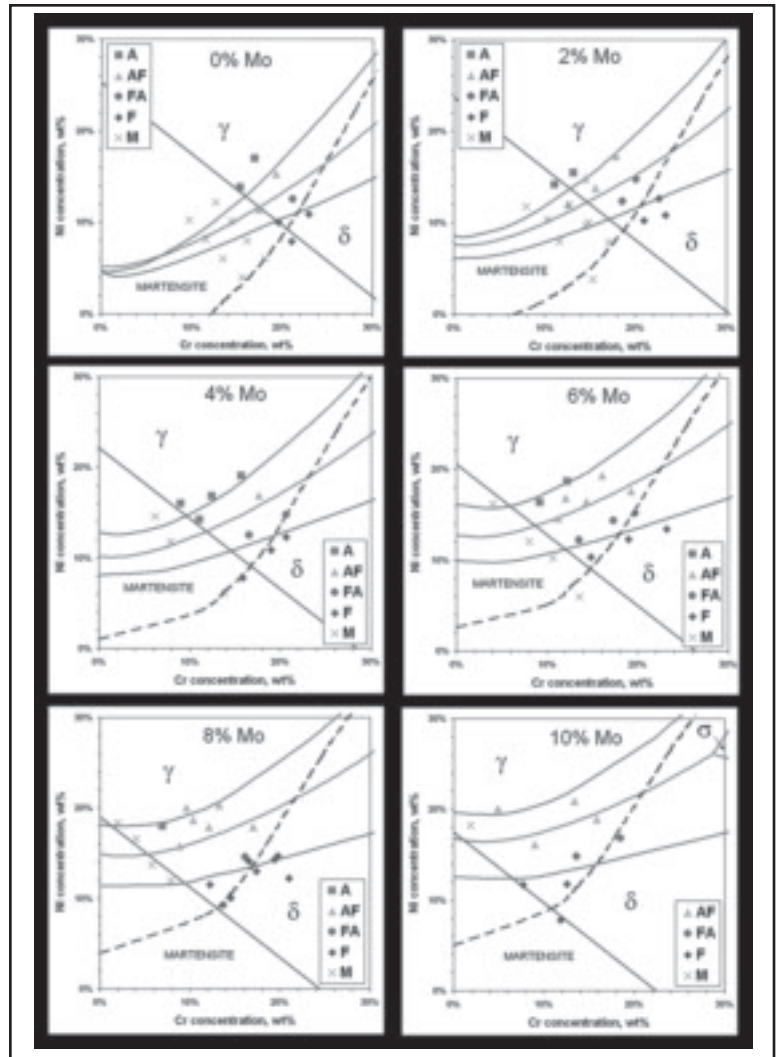


Fig. 2 — Multicomponent phase stability diagrams of the Fe-Ni-Cr-Mo quaternary system, for each level of Mo content studied. The data points in each diagram represent experimental alloy compositions, with the shape of the data point signifying the observed solidification mode. The measured wt-% ferrite for each composition is included alongside the respective data point.

tooling requires a large capital investment; and the high travel speeds required to induce dendrite tip undercooling and reduced levels of microsegregation also typically produce very small welds, and are thus not amenable to many practical joint designs and base metal thicknesses. Clearly, each of the current solutions for joining SASS alloys exhibit practical difficulties that can hinder their use in applications where good corrosion resistance of a welded assembly is critical.

One potential approach for reducing the problems of Mo microsegregation and solidification cracking in Mo-bearing SASS alloys is to design an alloy or filler metal that exhibits a primary ferrite solidification mode and subsequently transforms to austenite by a solid-state reaction. Such alloys are known to exist in the simple Fe-

Ni-Cr ternary system (Ref. 6). This solidification sequence provides two primary advantages. First, the primary ferrite solidification mode does not segregate Mo to the liquid. Rather, *Thermo-Calc* calculations show that ferrite is expected to be enriched in Mo, since the partition coefficient of Mo in ferrite is slightly greater than unity (Refs. 7, 8). The diffusion rates of substitutional alloying elements such as Mo and Cr are typically two orders of magnitude higher in ferrite than in austenite (Ref. 9). As a result, significant diffusion of Mo can occur during primary ferrite solidification and reduce or eliminate any Mo concentration gradient. The high diffusion rates will also permit the backdiffusion of nickel, which is segregated to the liquid by the solidifying ferrite. Second, ferrite is known (Refs. 10, 11) to exhibit

much higher solubility of the tramp elements P and S. These elements are known to cause solidification cracking due to the formation of P- and S-rich liquid films in the interdendritic and grain boundary regions at the end of solidification. Alloys that solidify in the primary ferrite mode are known (Ref. 10) to have significantly reduced susceptibility to solidification cracking due to the higher solubility of P and S and concomitant reduced amount of solute-rich liquid films.

The eventual development of alloys requires a sound understanding of the influence of composition on the phase transformation sequences and resultant microstructure. Thus, the objective of this research is to develop a basic understanding of microstructural evolution in Fe-Ni-Cr-Mo alloys that will serve as the basis for

development of SASS alloys with improved corrosion resistance and weldability. This paper describes the overall influence of alloy composition on the resulting microstructure. Details on various phase transformations observed from this research can be found in Refs. 12 and 13.

## Experimental Procedure

Numerous vertical isopleths, such as that seen in Fig. 1A, were constructed of the Fe-Ni-Cr-Mo system using the CALPHAD software *Thermo-Calc* (Ref. 7) in conjunction with the Iron Alloy Database (Ref. 8). While calculations were performed with Mo additions of 0, 2, 4, 6, 8, and 10 wt-%, the number of possible phases present was limited to three: liquid, ferrite, and austenite. The only solid phases included in the calculations were ferrite and austenite, as these are the only primary solidification phases present in the composition space considered here. The  $\sigma$ -phase was included in later calculations in order to ascertain the development behavior of this phase, but was not included in the generation of phase stability diagrams in the following discussion. These calculations were used to generate composite phase stability diagrams that could be used to estimate the influence of alloy composition on the solidification mode, possible solid-state transformation, and resultant microstructure. Development and use of these diagrams is discussed in the next section.

Laboratory studies were conducted in order to verify the accuracy of the diagrams in predicting microstructural development and identify alloys that exhibited the desired transformation sequence described above. A total of 95 alloys with systematic variations in Ni and Cr across both sides of the eutectic line were prepared for each of the six nominal Mo compositions simulated using *Thermo-Calc*. A master alloy of Fe-28Cr together with virgin Fe, Ni, and Mo were combined using an arc-button melter (ABM), supplied by Thermal Technologies, Inc. The bell jar of the ABM was evacuated and backfilled with Ar shielding gas. A manually controlled gas tungsten arc welding (GTAW) torch running at 300 A and 10 V inside the chamber was manipulated to melt the elemental components on a water-cooled Cu hearth. The target alloy compositions are shown in Table 1. The ~50-g buttons were subject to metallographic preparation and subsequent microstructural analysis in order to reveal and identify the particular solidification mode and solid-state transformation mechanisms. The relative locations and shape of the ferrite and austenite phases were used as indications of the solidification mode and morphological

**Table 1 — Nominal Compositions of Experimental Alloys, as Measured by Wet-Chemical Analysis<sup>(a)</sup>**

Target	Fe	Ni	Cr	Mo	SM	wt-% Ferrite
0Mo-10Cr-10Ni	79.86	10.26	9.74	0	M	—
0Mo-12Cr-8Ni	80.16	8.12	11.56	0	M	—
0Mo-14Cr-6Ni	80.37	6.01	13.45	0	M	—
0Mo-16Cr-4Ni	80.23	3.97	15.59	0	M	—
0Mo-13Cr-12Ni	75.07	12.16	12.6	0	M	—
0Mo-15Cr-10Ni	75.27	10.13	14.4	0	M	—
0Mo-17Cr-8Ni	75.71	7.97	16.1	0	M	—
0Mo-19Cr-6Ni	75.64	6.01	18.09	0.01	M	—
0Mo-16Cr-14Ni	70.61	13.85	15.34	0.01	A	0
0Mo-18Cr-12Ni	70.86	11.45	17.43	0.02	AF	2.289
0Mo-20Cr-10Ni	70.14	10.02	19.59	0.02	F	10.53
0Mo-22Cr-8Ni	70.77	7.89	21.06	0.01	F	55.13
0Mo-18Cr-17Ni	65.69	17.01	16.98	0.01	A	0
0Mo-20Cr-15Ni	65.1	15.3	19.32	0.01	AF	0.2175
0Mo-22Cr-13Ni	66	12.55	21.18	0.01	FA	9.205
0Mo-24Cr-11Ni	65.87	10.87	22.94	0.01	F	19.22
2Mo-8Cr-12Ni	78.36	11.77	7.96	1.78	M	—
2Mo-10Cr-10Ni	77.39	10.33	10.27	1.86	M	—
2Mo-12Cr-8Ni	73.52	9.7	14.55	2.05	M	—
2Mo-16Cr-4Ni	78.96	3.85	15.31	1.66	M	—
2Mo-11Cr-14Ni	72.78	14.16	11.1	1.79	A	0
2Mo-13Cr-12Ni	73.35	11.96	12.71	1.78	M	—
2Mo-15Cr-10Ni	73.54	10.04	14.8	1.4	M	—
2Mo-17Cr-8Ni	73.11	7.88	17.06	1.71	M	—
2Mo-14Cr-16Ni	69.45	15.49	13.19	1.57	A	0
2Mo-16Cr-14Ni	68.24	13.76	15.58	2.19	AF	0.617
2Mo-18Cr-12Ni	66.31	12.6	18.55	2.22	FA	7.925
2Mo-20Cr-10Ni	66.91	10.26	20.92	1.6	F	15.33
2Mo-18Cr-17Ni	62.14	17.3	17.86	2.39	AF	0.178
2Mo-20Cr-15Ni	62.17	15.02	20.33	2.12	FA	5.395
2Mo-22Cr-13Ni	62.44	12.65	22.6	1.97	F	14.17
2Mo-24Cr-11Ni	63.75	10.85	23.3	1.78	F	50.255
4Mo-6Cr-14Ni	75.73	14.59	6.18	3.37	M	—
4Mo-8Cr-12Ni	76.77	11.81	7.92	3.36	M	—
4Mo-12Cr-8Ni	77.33	7.95	11.64	2.9	M	—
4Mo-14Cr-6Ni	76.61	6.06	13.85	3.28	M	—
4Mo-9Cr-16Ni	71.31	15.99	9	3.55	A	0
4Mo-11Cr-14Ni	71.08	14.21	11.06	3.46	A	0
4Mo-13Cr-12Ni	72.58	11.99	12.55	2.68	AF	1.397
4Mo-17Cr-8Ni	72.99	7.8	15.83	3.13	F	50.52
4Mo-13Cr-17Ni	67.28	16.82	12.43	3.27	A	0
4Mo-15Cr-15Ni	67.9	14.83	14.46	2.58	AF	0.375
4Mo-17Cr-13Ni	66.59	12.51	16.57	3.95	FA	7.31
4Mo-19Cr-11Ni	66.42	10.88	18.98	3.42	F	17.835
4Mo-16Cr-19Ni	61.08	19.05	15.68	3.95	A	0
4Mo-18Cr-17Ni	61.58	16.88	17.6	3.67	AF	0.7245
4Mo-20Cr-15Ni	59.91	14.75	20.63	4.26	FA	9.815
4Mo-22Cr-13Ni	62.91	12.31	20.62	3.79	F	17.42
6Mo-4Cr-16Ni	73.57	16.2	4.02	5.98	M	—
6Mo-8Cr-12Ni	73.88	12.02	8.01	5.84	M	—
6Mo-10Cr-10Ni	73.6	10.21	10.64	5.27	M	—
6Mo-14Cr-6Ni	74.41	5.95	13.59	5.72	M	—
6Mo-9Cr-16Ni	68.73	16.33	9.18	5.58	A	0
6Mo-11Cr-14Ni	68.66	14.57	11.2	5.29	AF	0.184
6Mo-13Cr-12Ni	68.06	12.23	13.53	5.87	FA	5.33
6Mo-15Cr-10Ni	69.01	10.31	14.83	5.48	F	13.025
6Mo-12Cr-18Ni	63.37	18.64	12.2	5.48	A	0
6Mo-14Cr-16Ni	63.55	16.4	14.37	5.36	AF	0.148
6Mo-16Cr-14Ni	62.25	14.37	17.29	5.75	FA	6.475
6Mo-18Cr-12Ni	62.93	12.31	18.97	5.44	F	14.385
6Mo-16Cr-19Ni	58.52	19.31	16.08	5.74	AF	0
6Mo-18Cr-17Ni	57.39	17.57	19.26	5.41	AF	0.5125
6Mo-20Cr-15Ni	58.77	15.18	19.7	5.95	F	12.18
6Mo-22Cr-13Ni	57.05	13.41	23.17	5.94	F	38.92

(a) All values are expressed in weight percent. The solidification mode and measured weight percentage of ferrite of the alloy is listed, unless the alloy was found to contain martensite. (A=austenite, AF=austenite-ferrite, FA=ferrite-austenite, F=ferrite, M=martensite.)

— continued on page 285-s

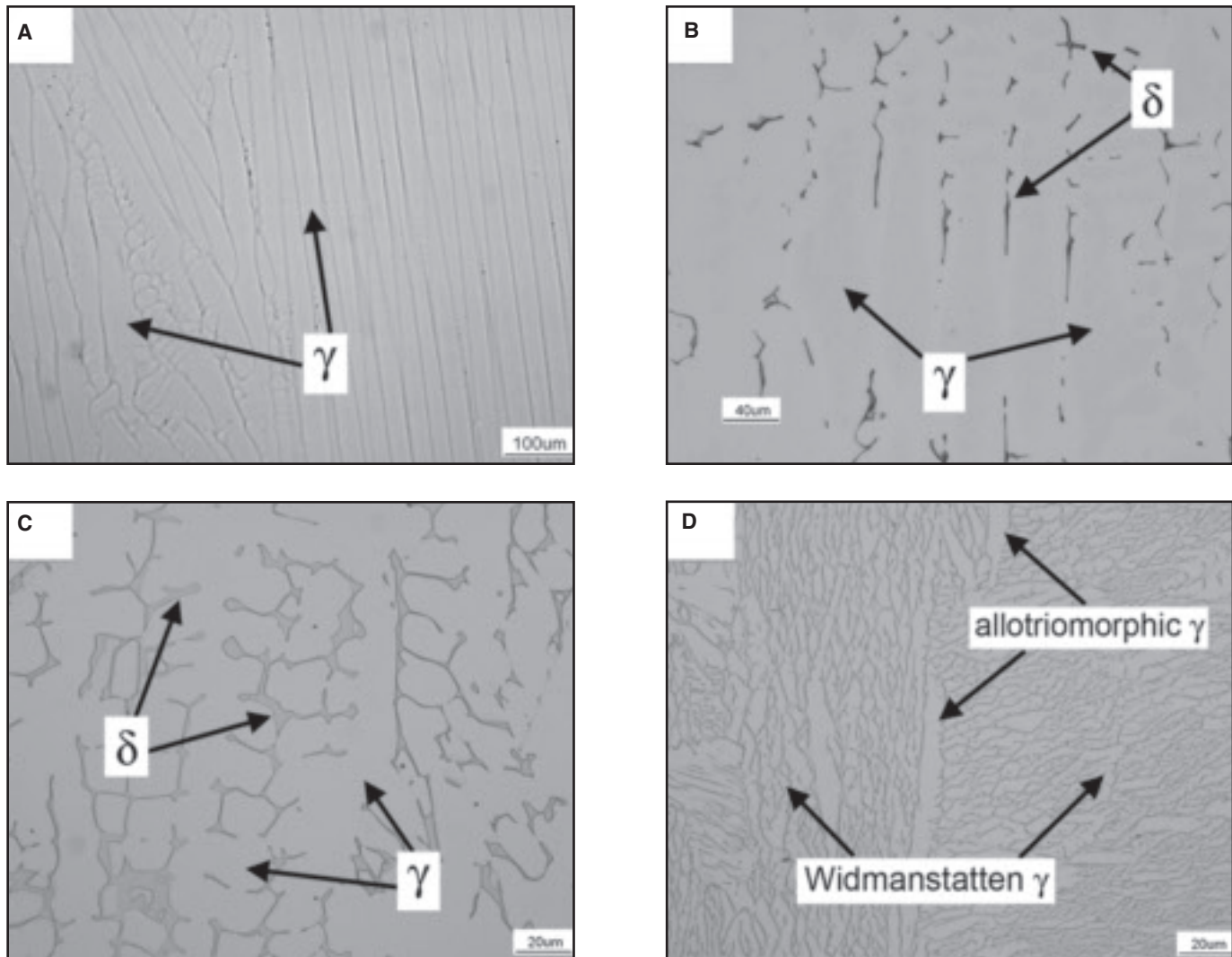


Fig. 3 — Representative microstructures of the four solidification modes observed in the set of Fe-Ni-Cr-Mo alloys generated in this study. A — A mode: 0Mo-18Cr-17Ni; B — AF mode: 0Mo-18Cr-12Ni; C — FA mode: 2Mo-18Cr-12Ni; D — F mode: 2Mo-17Cr-8Ni.

type in a manner previously described by Elmer (Ref. 14). A Feritscope®, manufactured by Fischer Technology, Inc., was used to determine the specific weight percentage of ferrite within each alloy button. In addition, the Ferrite Number (FN) was measured from the set of samples known to solidify as primary ferrite for the purposes of comparison with the WRC-1992 weld constitution diagram. Precision was maintained for both sets of measurements through the use of calibrated standards of known ferrite content.

Experiments were also performed to study the influence of increased cooling rates on the type and degree of solid-state transformations that would occur through the use of high-energy-density (HED) welds. Autogenous laser welds were conducted using a 700-W Nd-YAG laser (measured at 370 W at the weld surface) at travel speeds of 10, 50, and 100 in./min (4.2, 21, and 42 mm/s, respectively). The

laser weld passes introduced significantly higher cooling rates relative to that in the ABM method. The following sections focus entirely on results accumulated from the arc button microstructures, while the results of microstructural analysis of the laser welds is discussed in the last section.

Dendrite arm spacing measurements were used to estimate the cooling rate associated with the ABM and laser welding conditions. The relationship between dendrite arm spacing  $\lambda$  and cooling rate  $\epsilon$  has been determined (Ref. 15) for 310 stainless steel and is given by the following:

$$\lambda = 80\epsilon^{-0.3}$$

Several alloys were selected with similar composition and identical solidification mode (austenite) as 310 stainless steel in order to use the expression above to estimate the cooling rate. Although

austenitic stainless steels possess lower thermal conductivities than ferritic stainless steels, it is assumed there was no large change in thermal properties over the range of composition studied.

Electron probe microanalysis (EPMA) was conducted on select alloys for each of the observed solidification modes in order to measure the distribution of each element within the microstructure. Raw data were converted to concentration values using the correction scheme devised by Heinrich (Ref. 16). EPMA was also conducted on several of the HED weld zones to determine elemental distribution. Positive phase identification was carried out using backscattered electron Kikuchi pattern (BEKP) analysis on the microstructures of both the ABM button and the laser weld passes. This technique captures an image of the diffraction pattern of backscattered electrons while the sample undergoes SEM photomicrography. Indexing of the pattern

reveals the crystal structure characteristic of the phase (fcc:  $\gamma$ -austenite, bcc:  $\delta$ -ferrite, tetragonal:  $\sigma$ -phase).

## Results and Discussion

### Phase Stability Diagrams

Specific points of interest in the calculated vertical isopleths were used to generate the phase stability diagrams. As shown in Fig. 1A, the compositions of the eutectic point and the maximum solubility of Cr in austenite were taken from pseudo-binary phase diagram at various concentrations of Fe. Alloy compositions to the right of the eutectic point will solidify as ferrite (assuming negligible dendrite tip undercooling), while compositions to the left of the maximum solid solubility of Cr in austenite have the thermodynamic potential for the ferrite-to-austenite transformation to go to completion. Thus, alloys between these two key points represent the range of compositions that can potentially exhibit the desired phase transformation sequence. When plotted on the axes of Ni and Cr concentration, similar to a liquidus projection, these two points form lines that bound the range of desired compositions. An example of a multicomponent phase stability diagram is shown in Fig. 1B. The band across the center describes the three vertices of the eutectic triangle. The dashed line that intersects this band represents the maximum solubility of Cr in austenite, which curves below the eutectic triangle at high Cr and Ni concentrations. This computational approach can be used to bound a wide range of compositions that have the thermodynamic potential to develop an austenitic matrix that is preceded by ferrite solidification. Since the diagrams take into account only thermodynamic considerations, they are not proficient at predicting the mechanism or amount of transformation that will occur. This factor can only be found through an analysis of the kinetics of the system, which considers the cooling conditions present. Therefore, the diagrams represent a necessary, but not sufficient, condition for attaining an austenitic matrix alloy derived from ferritic solidification.

Compositions that meet both requirements have been shaded for emphasis in both Fig. 1A and B. The martensite line derived from the Schaeffler diagram is also included, the basis for which is described below. The range of compositions that can be viewed simultaneously is greater in this multicomponent phase stability diagram than in the vertical isopleths. Figure 2 shows the entire array of phase stability diagrams generated in this study for each Mo content. The data points on each represent the experimental alloys, the characterization results of

**Table 1 — Continued**

Target	Fe	Ni	Cr	Mo	SM	wt-% Ferrite
8Mo-2Cr-18Ni	71.31	18.34	1.96	8.29	M	—
8Mo-6Cr-14Ni	72.11	13.72	5.75	8.27	M	—
8Mo-8Cr-12Ni	71.94	11.99	7.91	7.99	M	—
8Mo-12Cr-8Ni	—	—	—	—	—	—
8Mo-7Cr-18Ni	66.76	18.02	6.91	8.15	A	0
8Mo-9Cr-16Ni	67.03	15.75	8.82	8.22	AF	0
8Mo-13Cr-12Ni	68.7	11.49	12.24	7.12	F	3.03
8Mo-15Cr-10Ni	69.12	9.3	13.71	7.61	F	26.89
8Mo-11Cr-19Ni	62.57	18.66	10.39	8.18	AF	0
8Mo-13Cr-17Ni	63.86	16.86	12.06	6.99	AF	0
8Mo-15Cr-15Ni	60.53	14.58	16.11	8.24	FA	1.92
8Mo-17Cr-13Ni	61.3	13.01	17.38	7.83	F	14.51
8Mo-14Cr-21Ni	58.1	20.3	13.21	8.14	AF	0
8Mo-17Cr-18Ni	57.71	17.88	17.03	7.08	AF	0
8Mo-20Cr-15Ni	58.1	14.32	19.4	7.85	F	13.17
8Mo-22Cr-13Ni	58.94	12.22	20.97	7.52	F	48.15
10Mo-2Cr-18Ni	69.44	18.24	1.92	10.29	M	—
10Mo-4Cr-16Ni	70.48	16.59	4.06	8.73	M	—
10Mo-8Cr-12Ni	70.36	11.69	7.71	10.06	F	8.025
10Mo-12Cr-8Ni	69.79	7.78	11.83	10.37	F	65.76
10Mo-5Cr-20Ni	64.88	20.08	4.93	9.96	AF	0
10Mo-9Cr-16Ni	65.3	16.14	8.98	9.39	AF	0
10Mo-13Cr-12Ni	65.69	11.76	12.56	9.42	F	4.8
10Mo-15Cr-10Ni	66.14	10.05	14.55	8.94	F	40.63
10Mo-10Cr-20Ni	62.92	20.02	9.63	7.22	AF	0
10Mo-12Cr-18Ni	62.21	17.92	12.1	7.71	AF	0
10Mo-14Cr-16Ni	61.1	14.82	13.59	9.86	FA	0.3995
10Mo-16Cr-14Ni	61.29	14.1	16.57	8.55	F	8.97
10Mo-14Cr-21Ni	55.73	20.9	13.37	9.74	AF	0
10Mo-16Cr-19Ni	54.8	18.88	15.84	10.18	AF	0
10Mo-18Cr-17Ni	53.08	16.84	18.44	10.95	FA	0
10Mo-20Cr-15Ni	56.66	14.69	19.72	8.51	F	8.355

**Table 2 — Cell Spacing Measurements Used to Calculate Cooling Conditions in the Arc-Melt and HED Weld Conditions**

Melt	Travel Speed (mm/s)	$\lambda$ ( $\mu$ m)	St. Dev. ( $\mu$ m)	$\epsilon$ (K/s)
Button	—	27	7	30
LW1	4.2	2.6	0.3	$3 \times 10^4$
LW2	21	1.8	0.2	$1 \times 10^5$
LW3	42	1.4	0.2	$2 \times 10^5$

which are discussed in more detail below. Successively higher additions of Mo cause the eutectic triangle not only to widen, but also to shift its location toward higher Ni contents. The latter effect is a result of the ferrite-stabilizing effect of Mo comparable to that of Cr. In addition, the continued addition of Mo widens the space between the eutectic and the boundary representing the maximum solubility of Cr in austenite, thereby broadening the range of compositions with the potential to exhibit the target behavior. The phase stability diagrams calculated in this research were validated using metallographic observations of each alloy. The results of the experimental alloy data are placed on the phase stability diagram with the nearest Mo content at the Cr and Ni contents measured via wet chemical techniques. The type of solidification mode is denoted by the shape of the data point. The target

compositions for the alloys, the actual measured compositions, the resulting solidification mode, and the measured weight-percent ferrite can be seen in Table 1. Alloys containing martensite are noted as such in place of the solidification mode, and the corresponding ferrite contents are omitted since the measurements experienced interference from the magnetic signature of martensite.

The calculated eutectic lines were fairly accurate in separating alloys between the austenitic and ferritic primary solidification modes, especially in the lower Mo diagrams. Although the eutectic line is seen to curve, it runs nearly parallel to a  $Cr_{eq}/Ni$  ratio of 1.5 over the compositional range of the experimental alloys. Nearly a third of the samples showed evidence of the martensite phase, as predicted by the Schaeffler diagram. The first indication of the presence of martensite was given by

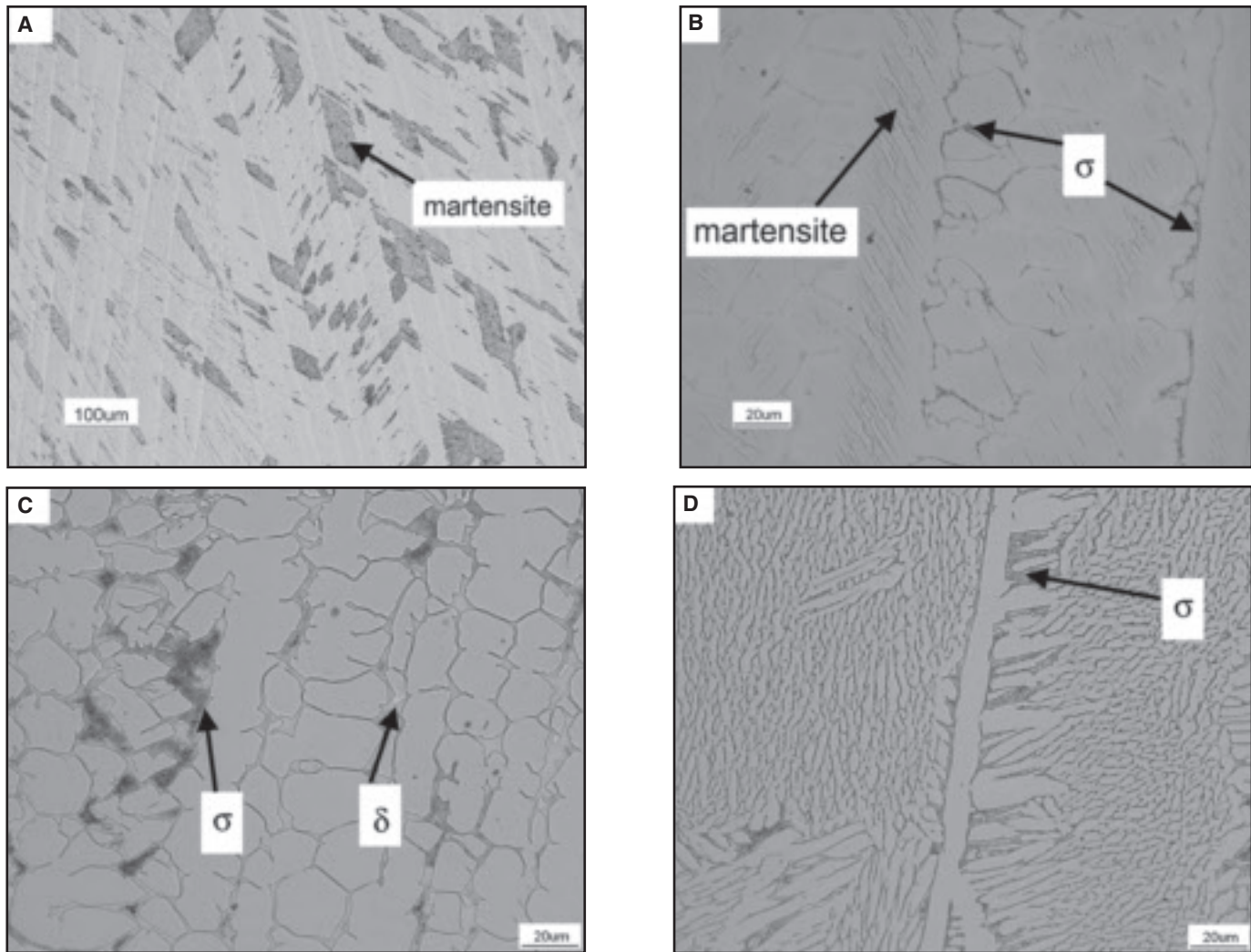


Fig. 4 — Arc-melt microstructures of secondary solid-state transformations that occurred in the set of Fe-Ni-Cr-Mo alloys: A — A mode with martensite: 2Mo-8Cr-12Ni; B — AF mode with martensite and  $\gamma/\sigma$  eutectoid: 8Mo-13Cr-17Ni; C — FA mode with  $\gamma/\sigma$  eutectoid: 10Mo-18Cr-17Ni; D — F mode with  $\gamma/\sigma$  eutectoid: 10Mo-18Cr-17Ni.

the abnormally high magnetic signal in these alloys, which could be attributed to the magnetic properties of martensite; metallographic observations confirmed the presence of this phase. After martensite was identified, the Schaeffler martensite line was added to the phase stability diagrams to further confine the range of desired compositions. This boundary was found to provide a good estimation of compositions that are expected to form martensite. Since the martensite phase was not desirable in this particular application, microstructural analysis of these 28 alloys is omitted in order to maintain focus on alloys composed predominately of austenite. A separate article (Ref. 12) discusses the myriad microstructural development sequences involving martensite that are possible in this alloy system. Of the 67 alloys that contained no martensite, only 6 were found to disagree with the primary solidification modes predicted by the

phase stability diagrams. In all cases, their nominal compositions were very close to the calculated eutectic lines.

#### Weld Metal Microstructures

A detailed description of the wide range of transformation sequences and resultant microstructures of the experimental alloys is presented elsewhere (Ref. 12), and only a summary of the pertinent results are provided here. The matrix of alloys was shown to contain each of the four common solidification modes exhibited by stainless steels: 1) austenitic (A); 2) austenitic-ferritic (AF); 3) ferritic-austenitic (FA); and 4) ferritic (F). A representative microstructure for each of these modes can be seen in Fig. 3. The first two images in Fig. 3A and B show alloys with austenitic primary solidification modes. The A mode alloy in Fig. 3A is entirely austenite, while the AF mode alloy

in Fig. 3B contains interdendritic ferrite as a result of eutectic solidification. Solidification mode determination of primary austenite alloys can be difficult, as eutectic ferrite in AF mode alloys may be purged by subsequent solid-state transformation. In this work, only those alloys that emitted a magnetic signature (measured with the ferrite detector) or otherwise showed microstructural evidence of ferrite (see below) were designated with the AF mode.

The primary ferrite solidification modes were of greatest importance in this study, since they fulfill the requirements set forth previously. The difference between the two modes is the existence of austenite at the end of solidification. FA mode alloys exhibit this interdendritic austenite, from which the solid-state transformation of ferrite into austenite may ensue epitaxially (Ref. 14). A representative microstructure of the FA mode

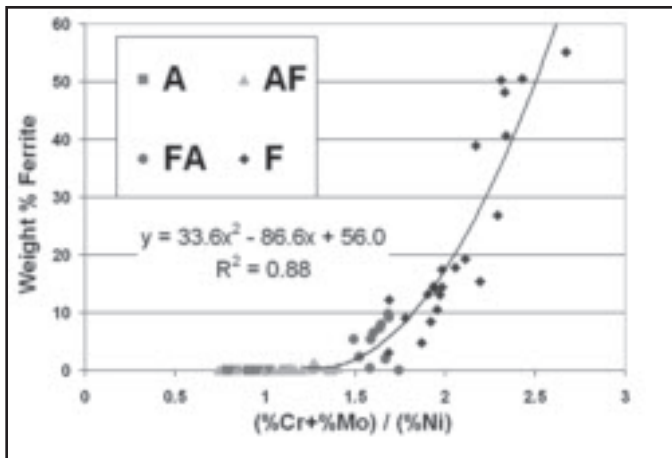


Fig. 5 — The effect of  $Cr_{eq}/Ni$  ratio on the measured weight percent of ferrite. The data points are separated by the type of solidification mode.

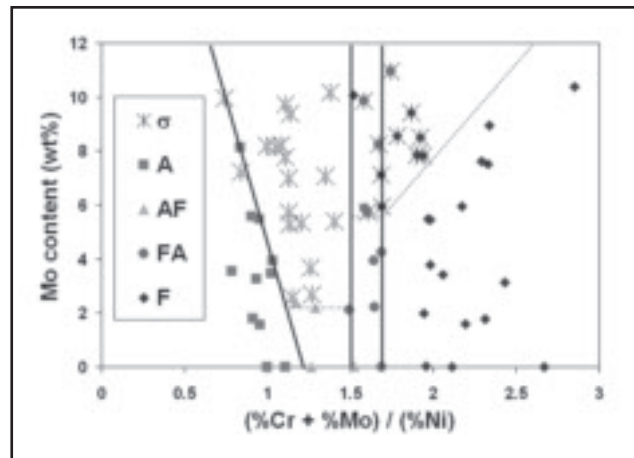


Fig. 6 — Microstructural map of alloy solidification mode based on  $Cr_{eq}/Ni$  ratio and Mo content. Boundaries are included to separate regions by solidification mode and  $\sigma$ -content.

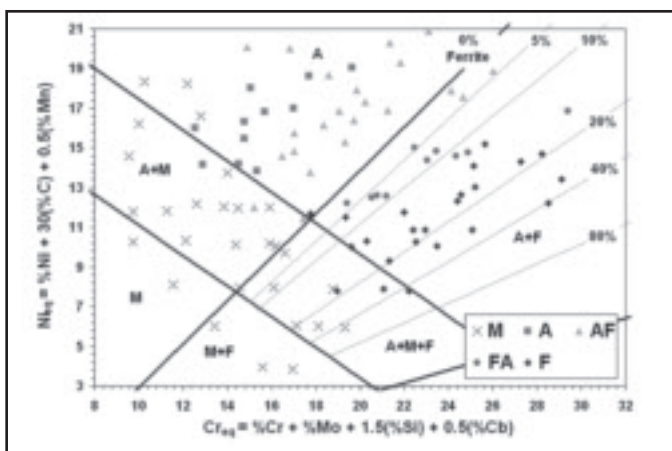


Fig. 7 — The Schaeffler 1949 weld constitution diagram, with the entire set of experimental alloys plotted by nominal composition.

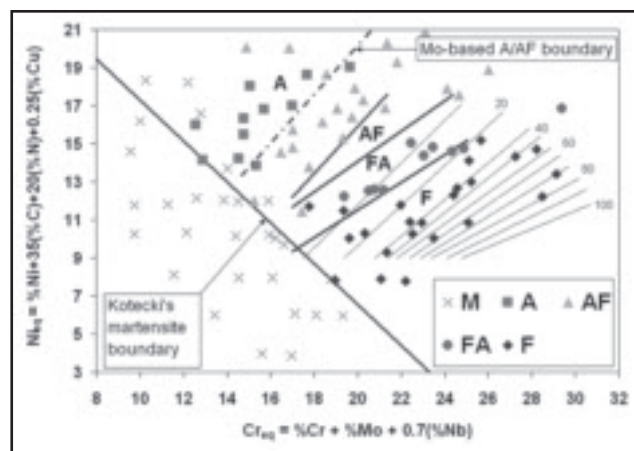


Fig. 8 — Experimental Fe-Ni-Cr-Mo alloys plotted on the WRC-1992 weld constitution diagram. The martensite boundary previously proposed by Kotecki (Ref. 20) is included. A new boundary is also given that divides A and AF mode alloys that contain significant amounts of Mo.

is shown in Fig. 3C. The residual ferrite seen in the structure is located at what were formerly the dendrite cores. Accordingly, the centerline of the austenite regions represents the former location of interdendritic regions. The compositions of all FA mode alloys were found to fall in the prescribed region of the phase stability diagram between the eutectic line and the maximum solubility of Cr in austenite.

The rest of the primary ferrite alloys belonged to the F mode group. An example of an F mode structure is shown in Fig. 3D. Fully ferritic grains were consumed by austenitic allotriomorphs at the grain boundaries, from which austenitic Widmanstätten side-platelets grew. Results of ferrite measurements indicate that this transformation mechanism is not as proficient as the FA mode at reducing the amount of residual ferrite. This is due to a lack of solidified ferrite in the structure, so

nucleation of this phase is first required. Eleven alloys were observed to solidify in the FA mode compositions; the ferrite contents were nearly all below that measured in the F mode samples.

Of special note is the reduction in ferrite content in primary ferrite samples as the Mo content is increased. Indeed, several 10 wt-% Mo F-mode samples contain less than 10 wt-% ferrite, and one FA alloy with 10 wt-% Mo produced a reading of 0 wt-% ferrite. Microstructural examina-

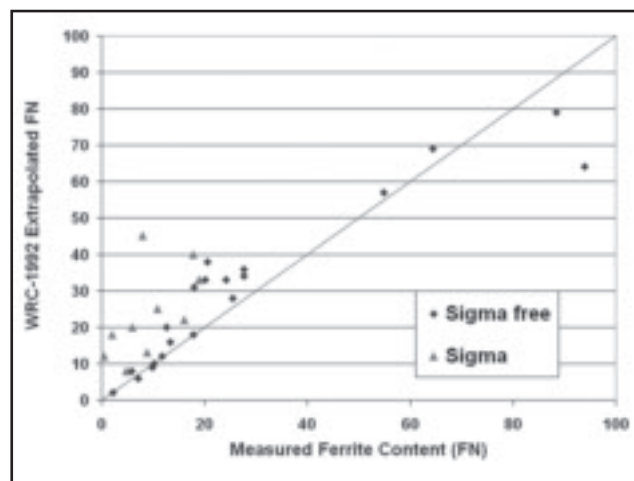


Fig. 9 — Comparison of experimental Ferrite Number (FN) measured via Ferriscope® and the FN predicted by the WRC-1992 diagram.

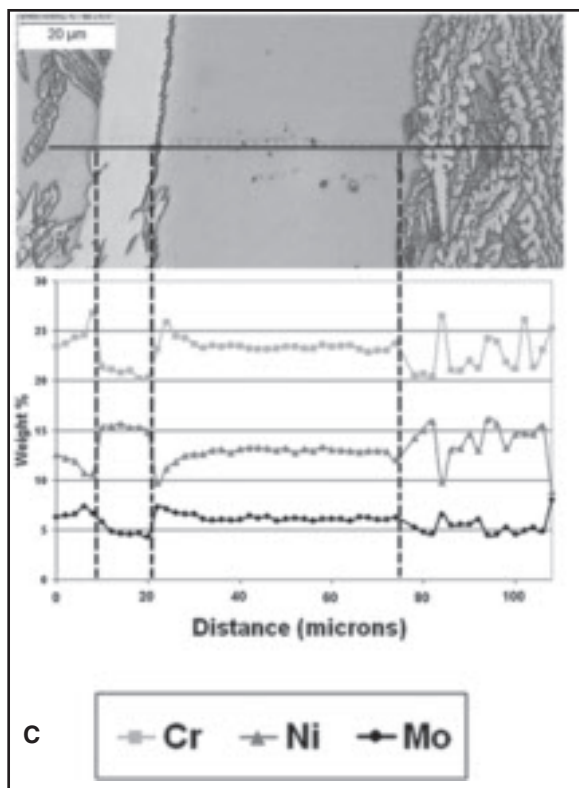
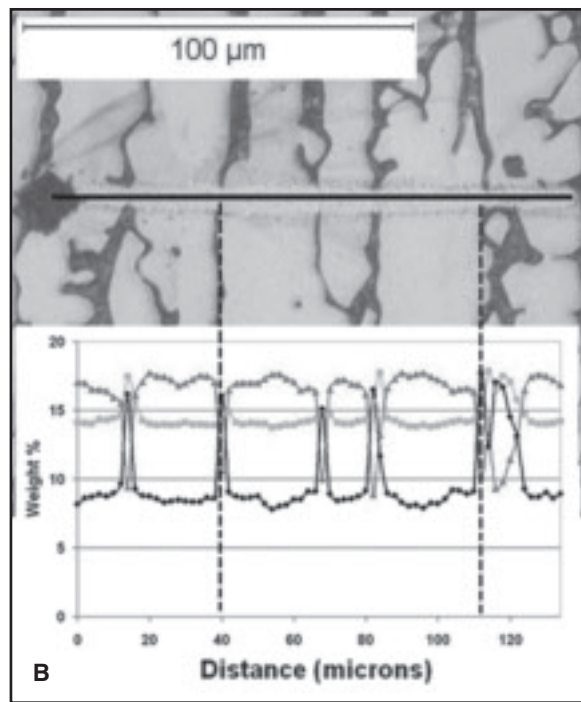
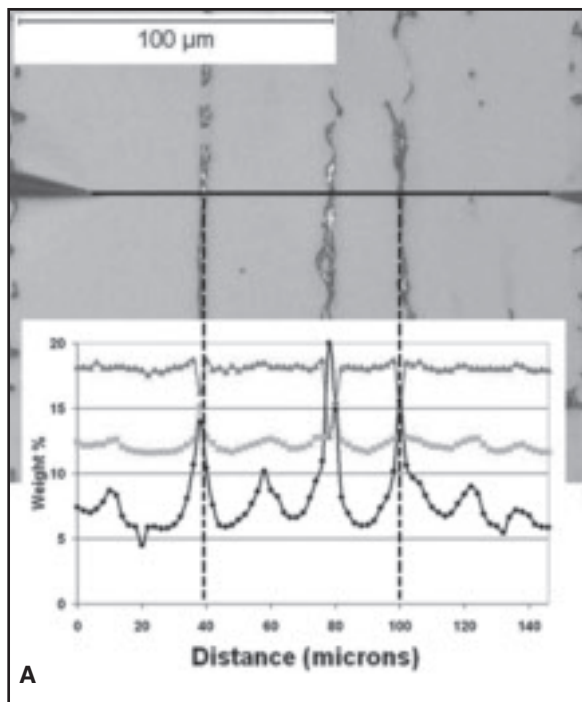


Fig. 10 — EPMA linescan data of the following: A — Solidified austenite cells with interdendritic eutectic ferrite and eutectoid  $\sigma$ -phases produced by AF solidification mode (10Mo-12Cr-18Ni); B — solid-state transformation product austenite with eutectoid  $\sigma$ -phase in the residual ferrite, produced by FA solidification mode (10Mo-14Cr-16Ni); C — austenitic allotriomorph and Widmanstätten platelets bordering a ferrite grain (6Mo-22Cr-13Ni).

tion of these regions revealed the presence of another phase: the high-Mo intermetallic  $\sigma$ -phase. Figure 4 shows light optical photomicrographs of microstructures associated with the formation of both sigma ( $\sigma$ ) and martensite. Positive phase identification of the  $\sigma$ -phase was made through BEKP results (Refs. 12, 13). Previous research has shown that a eutectoid  $\sigma/\gamma$  constituent may nucleate and grow from the parent ferrite phase (Refs. 17, 18). This eutectoid structure is observed in several solidification modes: AF (Fig. 4B), FA (Fig. 4C), and F (Fig. 4D). Such a structure is typically associated with annealing heat treatments that expose stainless steel ferrite to elevated temperatures for long durations. However, the high Mo contents of these alloys coupled with the cooling conditions of the ABM were sufficient for this eutectoid transformation to occur under the conditions studied here. The dissolution of the eutectoid constituent in the HAZ of laser welds and its presence in the residual ferrite of primary ferrite solidification microstructures indicated that it was the product of a solid-state transforma-

tion, and not as a solidification product. A more detailed description of the  $\delta \rightarrow \gamma + \sigma$  transformation observed in these alloys is available elsewhere (Ref. 13). The presence of the eutectoid constituent was also used as a secondary criterion for identifying AF mode alloys, as this transformation requires a ferritic parent phase. Therefore, several alloys containing 0.0 wt-% ferrite were labeled as AF mode due to the transformation of the interdendritic ferrite into the  $\sigma + \gamma$  eutectoid constituent.

The austenitic cell spacing measurements are summarized in Table 2. It was observed that the cell spacing increased through the thickness of the button. The region closest to the Cu hearth experienced the fastest cooling, which led to the smallest dendrites observed in the button. Accordingly, all data were acquired from the central band of the button in order to report the average cooling rate within the entire button. The photomicrographs given in Figs. 3 and 4 are from the same region of the arc-melt button. The data indicate an average cell spacing of 27  $\mu\text{m}$ , which represents an average cooling rate of approximately 30 K/s. This figure is within the range of casting and high-heat-input arc welding conditions (Ref. 14). This relatively low cooling rate would facilitate the nucleation and growth of the  $\gamma/\sigma$  eutectoid structure.

#### Effects of Composition on Microstructure and Ferrite Content

As would be expected, the weight percentage of ferrite measured in the alloys increased as a function of  $\text{Cr}_{\text{eq}}/\text{Ni}$  ( $\text{Cr}_{\text{eq}} =$

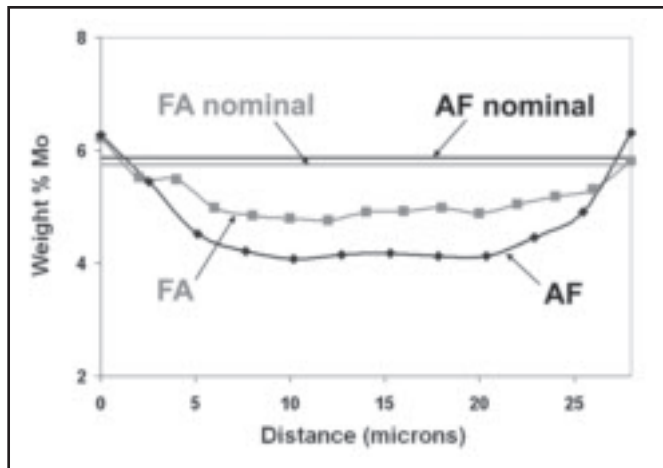


Fig. 11 — EPMA trace of the Mo content of a single austenite region. The FA trace (6Mo-16Cr-14Ni) consists entirely of solidified austenite, while the AF trace (6Mo-16Cr-14Ni) measures the Mo in both interdentritically solidified austenite and the austenite that grew epitaxially from it. The nominal Mo concentrations are also given for comparison.

wt-% Cr + wt-% Mo). These data are plotted in Fig. 5 with the alloys differentiated according to their solidification mode. These data indicate that each solidification mode belongs to a specific regime of  $Cr_{eq}/Ni$  ratio. The boundary between AF and FA mode alloys that is found at 1.5  $Cr_{eq}/Ni$  is in good agreement with previous findings (Ref. 10). Another significant boundary can be seen between FA and F mode alloys at  $\sim 1.7 Cr_{eq}/Ni$ . This value is slightly lower than the 1.9 Cr/Ni limit that was reported for Mo-free alloys by Elmer et al. (Ref. 14). The solidification mode boundaries in the literature were developed with chemically complex alloys, often containing C, Si, or Mn. The alloys studied herein represent simplified approximations of stainless steel compositions, which should be noted when making comparisons. The plot also shows that the FA mode was far more proficient at reducing the amount of the primary solidified ferrite, as the ferrite content in F mode alloys ranged between 3 and 55 wt-% while the ferrite content of FA alloys never surpassed 10 wt-%. A polynomial trendline has been included in this figure that relates the ferrite content to the  $Cr_{eq}/Ni$  ratio. Only those alloys with a detectable amount of ferrite were included in this relation.

The solidification mode and presence of  $\sigma$ -phase are mapped out as a function of Mo concentration and  $Cr_{eq}/Ni$  ratio in Fig. 6. As shown in Fig. 5, a switch in solidification mode from AF to FA occurs at a  $Cr_{eq}/Ni$  ratio of  $\sim 1.5$ . Also, the switch from FA to F mode is found at a  $Cr_{eq}/Ni$  ratio of  $\sim 1.7$ . Whereas the previous figure plotted all alloys by one compositional parameter ( $Cr_{eq}/Ni$ ), Fig. 6 shows that the previously observed boundaries that separate solidification modes do not change as

the Mo content is altered. These findings seem to indicate that the long-standing assumption that Mo possesses a ferrite-stabilizing strength equal to that of Cr is valid for the high-Mo alloys. Boundaries are also included that separate  $\sigma$ -containing samples from  $\sigma$ -free samples. Figure 6 thus represents a map by which microstructures may be predicted based on composition for a wide range of Mo-bearing stainless steels prepared under similar conditions. Of particular interest are the near-eutectic alloys with 4–6 wt-% Mo, characteristic of many commercially available alloys. Alloys that solidified in the AF mode showed substantial amounts of  $\sigma$ -phase that formed when the interdendritic ferrite decomposed to  $\sigma$ -phase via the  $\delta \rightarrow (\sigma + \gamma)$  eutectoid-type reaction. (Details of this transformation are provided in Ref. 13.) On the other side of the eutectic, FA mode alloys showed no evidence of  $\sigma$ -phase up to 6 wt-% Mo, save for a few isolated particles in the 6Mo-16Cr-14Ni sample.

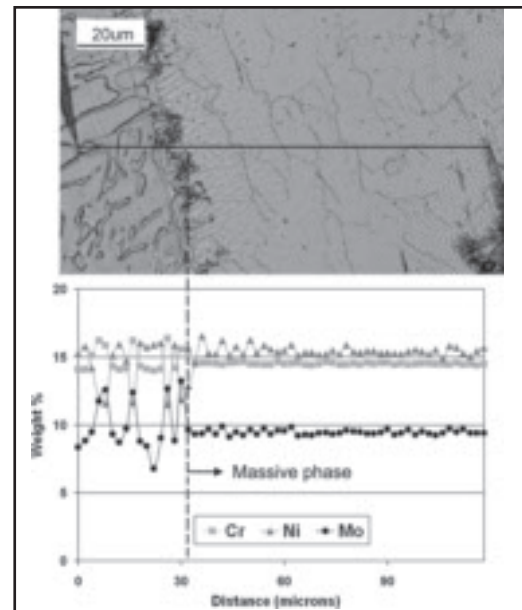


Fig. 12 — Representative microstructure and accompanying EPMA trace of 100 in./min HED weld in 10Mo-14Cr-16Ni sample.

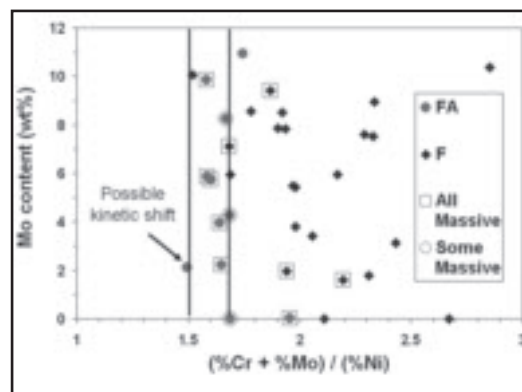


Fig. 13 — Microstructural map showing the incidence of the massive transformation as a function of composition and solidification mode. Alloys designated as experiencing “some” transformation contained massive product only in laser welds at 21 and 42 mm/s.

The lack of  $\sigma$ -phase in these 0–6 wt-% Mo alloys implies that the Mo content was more uniformly distributed throughout the microstructure as opposed to

**Table 3 — Six Candidate Mo-Bearing Stainless Steel Compositions, in wt-%, for the SASS Filler Metal Application. (All contain <10 wt-% ferrite and contain little to no  $\sigma$ -phase.)**

Designation	Fe	Ni	Cr	Mo	(Cr+Mo)/Ni	wt-% Ferrite
2Mo-18Cr-12Ni	66.31	12.6	18.55	2.22	1.648	7.93
2Mo-20Cr-15Ni	62.17	15.02	20.33	2.12	1.495	5.4
4Mo-17Cr-13Ni	66.59	12.51	16.57	3.95	1.640	7.31
4Mo-20Cr-15Ni	59.91	14.75	20.63	4.26	1.687	9.82
6Mo-13Cr-12Ni	68.06	12.23	13.53	5.87	1.586	5.33
6Mo-16Cr-14Ni	62.25	14.37	17.29	5.75	1.603	6.48

residing in the interdendritic regions forming  $\sigma$ -phase. This is confirmed quantitatively in a later section.

#### Comparison with Stainless Steel Weld Constitution Diagrams

Stainless steel constitution diagrams such as the Schaeffler diagram or WRC-1992 diagram are empirically derived tools for predicting the phase balance and ferrite content of stainless steel alloys based on the alloy composition, which is reduced to the simplified Cr and Ni equivalencies. The large number of alloys presented herein is useful in assessing the accuracy of these diagrams in predicting the microstructure of high (4–10 wt-%) Mo stainless steels.

The most modern constitution diagram is the WRC-1992 diagram (Ref. 19). The advantage of this diagram is its inclusion of boundaries that demarcate the various solidification modes available in the range of industrial stainless steels. Although previously included in the Schaeffler and DeLong diagrams, the WRC-1992 diagram does not include the martensite phase. The martensite boundary devised by Schaeffler in his diagram was superimposed on the stability diagrams shown in Fig. 2. This line was quite effective at separating martensite-free alloys from their martensite-containing counterparts, as shown in Fig. 7, which shows the entire set of experimental alloys plotted on the Schaeffler 1949 diagram. Numerous AF mode samples can be seen in the region of the Schaeffler diagram labeled as A (i.e., fully austenitic). This designation describes only the predicted microstructure — it is not a description of solidification mode as in the WRC-1992 diagram. A majority of these AF alloys were high-Mo samples that contained  $\sigma$ -phase. If the Mo was not present to enable the eutectoid transformation, it is possible that the interdendritic ferrite would have otherwise transformed into austenite, in effect creating the fully austenitic structure predicted by the diagram. However, the low partition coefficient of Mo causes it to be highly segregated to the liquid (Ref. 3). This in turn leads to a greater likelihood of forming interdendritic ferrite as compared to samples with equivalent amounts of Cr.

This effect can be seen as well in the WRC-1992 diagram, which is shown in Fig. 8. Plotting the samples according to solidification mode on the WRC-1992 diagram shows poor agreement between the predictions of the diagram and the experimentally observed solidification mode for primary austenite alloy compositions. The effects of Mo microsegregation are likely not accounted for in the WRC-1992 diagram, because the body of samples used in

the initial design suffers from a lack of high-Mo compositions (only four samples contained greater than 5 wt-% Mo, the highest reaching 6.85 wt-% Mo). Most of the AF alloys that disagree with the predictions of the WRC-1992 contain high concentrations of Mo. Thus, a new boundary is given in Fig. 8 to distinguish A and AF mode alloys with high (4–10 wt-%) Mo contents. Good agreement is shown, however, for the primary ferrite alloys. The diagram successfully predicted the solidification mode of these alloys since the bcc ferrite lattice is less likely to produce a segregated microstructure.

Recent research efforts have sought to locate a martensite line within the WRC-1992 diagram. Kotecki has proposed a martensite boundary (Ref. 20) (shown in Fig. 8) based mainly on the results of bend tests. The alloys that were found to contain martensite, based on both magnetic measurements and metallography, can be used to validate the boundary proposed by Kotecki. Five of the martensitic samples from this study are actually located above this boundary. All of these samples contain high amounts of Mo additions (>8 wt-%) and experienced austenitic solidification modes. The disagreement between Kotecki's boundary and these alloys can again be explained by the high potential for microsegregation of Mo. Visual cues given in the microstructure show that martensite rarely occurs in the interdendritic regions, and is typically localized in the dendrite cores (see Fig. 4A). Because of microsegregation, the Mo concentration at the core is actually less than the nominal composition. Thus, the incidence of martensite in these samples does not necessarily disagree with Kotecki's martensite boundary, since the true Mo concentration in the primary dendrite would shift the Cr equivalency of these areas to the left of the points demarcated in Fig. 8. Similarly, this explains the location of the four martensitic samples that exceed Schaeffler's martensite boundary, as seen in Fig. 7.

Another function of the WRC-1992 weld constitution diagram is its ability to estimate the ferrite content of a stainless steel alloy based on its composition. It uses the magnetically derived Ferrite Number (FN) value instead of weight-percent ferrite, as this parameter was found to be more reproducible. The FN of all primary ferrite, martensite-free alloys was measured for the purposes of comparison with the diagram. The results are displayed in Fig. 9. A fair amount of agreement is shown between the experimental FN and the predictions of the WRC-1992. By separating the data into  $\sigma$ -free and  $\sigma$ -containing alloys, the effects of the  $\delta \rightarrow (\sigma + \gamma)$  eutectoid transformation are high-

lighted. The measured ferrite content in  $\sigma$ -containing alloys was always less than that predicted by the model, which corroborates a solid-state transformation of the residual ferrite into the eutectoid constituent. Since the ferrite phase is consumed by this eutectoid transformation, it would logically follow that the measured FN values for these alloys would be less than predicted by the diagram.

#### Solute Redistribution

An example of the difference in solute profiles between alloys with similar Mo concentrations that form by AF and FA solidification are shown in Fig. 10A, B. The Mo profile shows a distinct increase in concentration across the distance between a cell core and the neighboring intercellular region produced by AF solidification. This was caused by the solidifying austenite cell rejecting Mo across the solid/liquid interface into the liquid. The solute accumulates in the intercellular region, since it is the last to solidify. During primary ferrite solidification, Mo is not segregated to the liquid. The austenitic regions produced by solid-state transformation in Fig. 10B show a more uniform concentration of Mo. Since the central axis of the austenite regions represents the former intercellular regions of the solidified ferrite structure, this observation is consistent with the lack of Mo segregation. The regions of elevated Mo concentration observed in the FA alloy shown are associated with the presence of  $\sigma$ -phase in this particular alloy.

The significant backdiffusion of solute in the ferrite phase is also verified in Fig. 10C, which shows the microstructure produced by F mode solidification. The central region of this solute profile shows the uniform distribution of all measured elements across a region of untransformed ferrite that encompasses several cell widths. The subsequent solid-state transformation from ferrite to allotriomorphic austenite caused a difference in Mo concentration between the austenite and residual ferrite. The partitioning of Mo during the  $\delta \rightarrow \gamma$  transformation is also apparent in Fig. 10B by the high levels of Mo seen in the  $\gamma/\sigma$  phase dual structure (recall that the  $\gamma/\sigma$  constituent forms from preexisting  $\delta$ -ferrite). As shown by peaks in the solute profile, the elements Cr and Mo, both stabilizers of the ferrite phase, were rejected into the residual ferrite during the  $\delta \rightarrow \gamma$  solid-state transformation process (again, this  $\delta$ -ferrite later transforms to  $\gamma/\sigma$ ). The austenite matrix resulting from the FA solidification mode contains slightly less than nominal, yet essentially uniform, concentrations of these solute atoms. Conversely, austenite-stabilizing Ni was drawn

into the newly created austenite, resulting in a uniform profile of Ni within the austenite that was greater than the nominal composition. As seen in Fig. 10B, the regions occupied by the eutectoid product are thus depleted of Ni.

Solute partitioning for a single austenitic transformation product can be examined using the grain boundary allotriomorph contained in Fig. 10C. While the concentrations of solute are relatively uniform within the allotriomorphic transformation product, there exist distinct differences in concentration between it and the neighboring ferrite grain. The amount of Mo and Cr are lower in the allotriomorph, while the amount of Ni has increased as a result of transformation. The ferrite nearest to the allotriomorph even shows elevated concentrations of Mo and Cr, the result of being partitioned to the parent ferrite. The general upheaval of concentration distribution brought about by solid-state transformations can also be seen on the right-hand side of the micrograph. The production of Widmanstätten austenite platelets has caused the uniform distribution of solute in the parent ferrite to be disrupted. Although the platelets are too small to be individually measured, the partitioning of solute is apparent in the measured chemical profile.

Solute partitioning resulting from the  $\delta \rightarrow \gamma$  solid-state transformation does not, however, cause a chemical gradient as high as that produced by microsegregation associated with austenitic (AF) solidification. Figure 11 compares the profile of Mo solute between a single solidified austenite cell brought about by AF solidification with a region of solid-state transformation austenite derived by the FA solidification mode. While neither austenite region reaches the nominal concentration of ~6 wt-% Mo, the concentration in the FA austenite is certainly closer to 6 wt-% across its entire width. The difference between the nominal and the core compositions is 1.74 wt-% for AF solidification, but a difference of only 0.88 wt-% Mo exists for the FA solidification mode.

### Candidate Alloys

It is worth noting that several alloys investigated in this research exhibited the desired FA solidification mode, a low ferrite content, and no  $\sigma$ -phase. Of the 67 alloys created that did not contain martensite, nine Mo-bearing alloys were identified that exhibited the FA solidification mode. Of these nine alloys, one contained 8 wt-% Mo and two contained 10 wt-% Mo. However, these three alloys all contained  $\sigma$ -phase. Since  $\sigma$ -phase is known for its unfavorable effects on mechanical properties and corrosion resis-

tance (Ref. 21), these three alloy compositions may not be optimal. The remaining six alloys, which are summarized in Table 3, contain only 5–10 wt-% of the ferrite phase, as measured by magnetic instrumentation, and provide a basis for promising candidate compositions for further study.

### Massive Transformation Structures

Several laser welds were deposited on each experimental alloy, with the travel speed being adjusted from 10 to 50 in./min to 100 in order to affect the cooling rate. As shown in Table 2, measurements of dendrite arm spacings in primary austenite samples indicated that cooling rates within the laser weld zones ranged from  $\sim 3 \times 10^4$  to  $2 \times 10^5$  °C/s, increasing with the travel speed. Each of the four solidification modes observed in the melt button samples were found in the laser welds. In nearly all cases, the solidification mode of the weld microstructure matched that of the button, indicating that the solidification velocities used here were not high enough to induce shifts in the solidification mode, with the possible exception of one alloy discussed below. More importantly, though, microstructural characterization revealed a subset of the weld structures that was found to experience a massive transformation of ferrite to austenite. This type of transformation, known to occur specifically at high cooling rates, causes no solute partitioning between the parent ferrite and product austenite phases and, under the correct set of processing conditions, can produce fully austenitic microstructures. Similar results have been observed in ternary Fe-Ni-Cr alloys (Refs. 6, 22). As shown in Fig. 12, a patchy morphology with irregular grain boundaries was observed that is characteristic of the massive product. Positive phase identification using backscattered electron Kikuchi (BEKP) patterns, the results of which can be found elsewhere (Ref. 23), confirmed that this was indeed the austenite phase. EPMA analyses were also performed on laser welds containing this patchy morphology. As shown by the example in Fig. 12, the massive product displays a uniform distribution of all alloying elements at the nominal levels. This segregation-free, fully austenitic structure should exhibit excellent corrosion resistance and toughness.

The solidification modes of the primary ferrite laser weld microstructures, which are susceptible to the massive transformation, have been plotted to show the compositional range over which the massive transformation was initiated in the laser welds. Figure 13 shows that the massive transformation is more likely to occur

in alloy compositions within a short  $Cr_{eq}/Ni$  range from the eutectic located at  $Cr_{eq}/Ni = 1.5$ . This appears to be associated with the compositional dependence of the  $T_o$  temperature, which is defined as the temperature at which both phases in a two-phase region of the phase diagram possess equivalent free energies. It is commonly held (Ref. 24) that, for the massive transformation to occur, this temperature must be surpassed during cooling before competing long-range diffusional transformations can occur. The compositional dependence of this value has a shape similar to the  $\delta + \gamma$  phase boundaries seen in Fig. 1A. Further discussion of the thermodynamics of the massive transformation as they pertain to these alloys can be found elsewhere (Ref. 23).

Three samples, labeled as “Some Massive” in Fig. 13, did not show evidence of the massive transformation until the laser weld travel speed was raised to 50 in./min (21 mm/s). The remainder of samples showed evidence of massive product in the microstructure of welds produced at all three travel speeds (labeled “All Massive” in Fig. 13). Interestingly, the FA mode alloy located directly on the eutectic line (2Mo-20Cr-15Ni) does not present any massive product. This is believed to be a consequence of a possible kinetic shift during solidification. While the button microstructure solidified as the FA mode, the elevated cooling rates in the HED weld zones resulted in dendrite tip undercooling that was sufficient to cause primary austenite solidification. The growth velocities present in these welds are similar to those found to cause kinetic shifts by Fukumoto and Kurz (Refs. 25–27). However, only the 2Mo-20Cr-15Ni composition was located close enough to the eutectic so as to be susceptible to a kinetic shift. Work performed by Fukumoto and Kurz on the Fe-Ni-Cr-C alloy system concluded that elements with a low partition coefficient (e.g., C and Mo) could alter the solidification behavior in near-eutectic alloys at high growth velocities (Ref. 26). Since the structure of this button was already austenite, there was no parent phase that could experience the massive transformation. Further investigations of this weld microstructure are necessary to determine whether this behavior can be attributed to a kinetic shift in solidification mode or localized compositional variation in a near-eutectic alloy such that AF solidification is favored.

### Conclusions

The phase transformations and resultant microstructures that form in Mo-bearing stainless steels have been evaluated over a wide range of Ni, Cr, and Mo

concentrations. The following conclusions can be drawn from this research:

1. The phase stability diagrams constructed from thermodynamic calculations provided a good predictive tool of solidification modes of Mo-bearing stainless steel alloys.

2. The ferrite content was shown to be a function of not only  $Cr_{eq}/Ni$  ratio, but also Mo concentration, specifically due to the transformation of ferrite into eutectoid  $\gamma + \sigma$  in high-Mo alloys.

3. The FA solidification mode produced a more uniform distribution of Mo solute in the transformed austenite phase than observed in the cores of solidified austenite cells produced by the AF mode.

4. The Schaeffler weld constitution diagram accurately predicted the presence of martensite in low-Mo alloys. The high microsegregation of Mo led to martensite forming in high-Mo alloys that exceeded Schaeffler's martensite boundary. For the same reasoning, several high-Mo alloys containing martensite exceed the martensite boundary proposed by Kotecki on the WRC-1992 diagram. Otherwise, these diagrams provide good accuracy of martensite prediction for high Mo alloys.

5. The location of numerous high-Mo AF mode alloys in the A mode region of the WRC-1992 diagram was attributed to microsegregation of Mo during solidification. The segregation of Mo solute to the liquid led to a larger amount of interdendritic ferrite. However, good agreement was shown for alloys that experience primary ferrite solidification.

6. The incidence of  $\sigma$ -phase formation in the high-Mo samples also led to inaccurate prediction of ferrite content by the WRC-1992 diagram for many of these alloys.

7. A massive transformation of  $\delta \rightarrow \gamma$  can produce fully austenitic microstructures with uniform distributions of Mo at the nominal concentration. The transformation is seen to occur in primary ferrite alloys that are near the eutectic composition.

8. Several alloys have been identified that solidify in the FA mode and have an austenite matrix with a more uniform distribution of Mo than that exhibited by primary austenite solidification. These alloys should have improved resistance to solidification cracking and localized corrosion.

#### Acknowledgments

The authors gratefully acknowledge financial support of this research by the Office of Naval Research, under Contract No. N00014-00-1-0448. Generous financial support was also provided by the AWS Foundation and the Navy Joining Center through an AWS Graduate Research Fel-

lowship. Some phase identification was performed at Sandia National Laboratories. Sandia National Laboratories is a multiprogram laboratory operated by Sandia Corporation, a Lockheed Martin Company, for the United States Department of Energy's National Nuclear Security Administration under contract DE-AC04-94AL85000.

#### References

- Banovic, S., DuPont, J., and Marder A. 2001. Dilution control in gas tungsten arc welds involving superaustenitic stainless steels and nickel based alloys. *Metallurgical and Material Transactions* 32B: 1171-1176.
- DuPont, J., Friedersdorf, L., Marder, A., and Banovic, S. 2001. Weldability and Corrosion Performance of Welds in AL-6XN Superaustenitic Stainless Steel. Lehigh University ATLSS Report No. 01-03. 2001.
- Banovic, S., DuPont, J., and Marder, A. Dilution and microsegregation in dissimilar metal welds between superaustenitic stainless steel and nickel base alloys. *Science and Technology of Welding and Joining* (UK) 7: 374-383.
- Banovic, S., DuPont, J., and Marder, A. 2003. Microstructural evolution and weldability of dissimilar welds between a superaustenitic stainless steel and nickel-based alloys. *Welding Journal* 82(6): 125-135.
- Perricone, M., and DuPont, J. 2003. Laser welding of superaustenitic stainless steel. *Trends in Welding Research: Proceedings of the 6th International Conference*. Materials Park, Ohio: ASM International. pp. 47-52.
- Brooks, J., Baskes, M., and Greulich, F. 1991. Solidification modeling and solid-state transformations in high-energy density stainless steel welds. *Metallurgical and Material Transactions* 22A: 915-926.
- Sundman, B. 2001. Thermo-Calc. S-100 44[[N]]. Stockholm, Sweden, Department of Materials Science and Engineering, KTH.
- Saunders, N. 2001. Fe-Data Thermodynamic Database. [[3.0]]. The Surrey Research Park, Guildford, UK, Thermotech, Ltd.
- Brooks, J., and Baskes, M. 1989. Microsegregation modeling and transformation in rapidly solidified austenite stainless steel welds. *Proceedings of the Second International Conference on Trends in Welding Research*, 153-158.
- Brooks, J., and Thompson, A. 1991. Microstructural development and solidification cracking susceptibility of austenitic stainless steel welds. *International Materials Reviews* 36, 16-44.
- Kou, S. 2003. *Welding Metallurgy*. Hoboken, N.J.: John Wiley & Sons, Inc.
- Anderson, T., DuPont, J., Perricone, M., and Marder, A. 2007. Phase transformations and microstructural evolution of Mo-bearing stainless steels. *Metallurgical and Materials Transactions* 38A: 86-99.
- Perricone, M., Anderson, T., Robino, C., DuPont, J., and Michael, J. 2007. Predicting Sigma Formation during Welding of Mo-Bearing Stainless Steels. Rio Grande Symposium on Advanced Materials '06.
- Elmer, J., Allen, S., and Eagar T. 1989. Microstructural development during solidification of stainless steel alloys. *Metallurgical and*

*Material Transactions* 20A: 2117-2131.

15. Katayama, S., and Matsunawa, A. 1984. *Proceedings of ICALCO*. pp. 60-67.

16. Heinrich, K., Mykleburst, R. L., Yakowitz, H., and Rasberry, S. D. 1972. Simple Correction Procedure for Quantitative Electron-Probe Microanalysis. NBS Technical Note 719, 1-31.

17. Reick, W., Pohl, M., and Dapilha, A. 1998. Recrystallization-transformation combined reactions during annealing of a cold rolled ferritic-austenitic duplex stainless steel. *ISIJ International* (Japan) 38, 567-571.

18. Shek, C., Shen, G., Lai, J., and Duggan, B. 1994. Early stages of decomposition of ferrite in duplex stainless steel. *Materials Science and Technology* 10, 306-311.

19. Kotecki, D., and Stewart, T. 1992. WRC-1992 constitution diagram for stainless steel weld metals: a modification of the WRC-1988 diagram. *Welding Journal* 71(5): 171-178.

20. Kotecki, D. 2000. A martensite boundary on the WRC-1992 diagram. *Welding Journal* 78(5): 180-192.

21. Koseki, T., and Ogawa, T. 1992. An investigation of weld solidification in Cr-Ni-Fe-Mo alloys. *Welding International* 6, 516-522.

22. Brooks, J., Headley, T., and Robino, C. 2000. Microstructure design for laser deposited 304L stainless steel. *Solid Freeform and Additive Fabrication: A Materials Research Society Symposium*. San Francisco, Calif.

23. Perricone, M., Anderson, T., DuPont, J., and Robino, C. 2006. On the massive transformation from ferrite to austenite in laser welded Mo-bearing stainless steels. *Materials Science & Technology '06*, Cincinnati, Ohio.

24. Aaronson, H. 2002. Mechanisms of the massive transformation. *Metallurgical and Materials Transactions* 33A: 2285-2297.

25. Fukumoto, S., and Kurz, W. 1997. The delta to gamma transition in Fe-Cr-Ni alloys during laser treatment. *ISIJ International* (Japan) 37, 677-684.

26. Fukumoto, S., and Kurz, W. 1998. Prediction of the delta to gamma transition in austenitic stainless steels during laser treatment. *ISIJ International* (Japan) 38, 71-77.

27. Fukumoto, S., and Kurz, W. 1999. Solidification phase and microstructure selection maps for Fe-Ni-Cr alloys. *ISIJ International* (Japan) 39, 1270-1279.